PNAS RESEARCH ARTICLE | ENGINEERING

# Low-grade wind-driven directional flow in anchored droplets

Shan Peng[a,1], Binglin Xie[b,1], Yanlei Wang[c,1], Mi Wang[c], Xiaoxin Chen[a], Xiaoyu Ji[a], Chenyang Zhao[a], Gang Lu[d], Dianyu Wang[e], Ruiran Hao[f], Mingzhan Wang[g], Nan Hu[b,h,2], Hongyan He[c,i,2], Yulong Ding[j], and Shuang Zheng[k,2]

Edited by Alexis Bell, University of California, Berkeley, CA; received March 1, 2023; accepted July 22, 2023

**Low-grade wind with airspeed $V_{wind}$ < 5 m/s, while distributed far more abundantly, is still challenging to extract because current turbine-based technologies require particular geography (e.g., wide-open land or off-shore regions) with year-round $V_{wind}$ > 5 m/s to effectively rotate the blades. Here, we report that low-speed airflow can sensitively enable directional flow within nanowire-anchored ionic liquid (IL) drops. Specifically, wind-induced air/liquid friction continuously raises directional leeward fluid transport in the upper portion, whereas three-phase contact line (TCL) pinning blocks further movement of IL. To remove excessive accumulation of IL near TCL, fluid dives, and headwind flow forms in the lower portion, as confirmed by microscope observation. Such stratified circulating flow within single drop can generate voltage output up to ~0.84 V, which we further scale up to ~60 V using drop "wind farms". Our results demonstrate a technology to tap the widespread low-grade wind as a reliable energy resource.**

wind energy | contact angle | wettability

## Significance

Wind energy, as a renewable power resource, is emerging due to the wide-spreading distribution and has supplied over 6% of the electricity consumption all over the world. However, low-speed wind (<5 m/s) is still challenging to extract using current technologies, which is far more abundant than high-speed wind. Here, we report a well-designed nanostructured surface that allows pinning and rotating of ionic liquid droplets under wind. It converts wind to electricity even when the speed is reduced to 0.2 m/s.

Recent decades have witnessed the explosive growth of global wind power capacity from 24 GW in 2001 to 840 GW in 2021 (over 7% of the world's electricity demand) because of its renewability, nonpollution, bargain price, ecological compatibility, and worldwide distribution, etc. (1–11). Currently, wind energy conversion uses wind turbines to transform airflow into mechanical rotation of specially designed blades, which finally actuates a generator for supplying electricity (2, 4, 12, 13). The power output $P_{wind}$ of turbine under wind velocity $V_{wind}$ (m/s) can be given by (4, 14, 15):

$$P_{wind} = \frac{\rho_{air} A_b C_p V_{wind}^3}{2}, \quad [1]$$

where $\rho_{air}$ is the air density (kg/m$^3$), $A_b$ is the swept area of the rotor blade (m$^2$), and $C_p$ denotes the power regulation coefficient. One can see from Eq. **1** that the $P_{wind}$ is proportional to the cube of $V_{wind}$ and a decrease in wind velocity will result in dramatical decline in power output (16). Unfortunately, high-speed wind is typically abundant only in open lands without obstacles, such as offshore platforms and mountain tops (17–20). Land areas with averaged wind speed less than 5 m/s are far richer and more widely distributed (*SI Appendix*, Fig. S1) (21–23), including forests and urban areas, where trees and building structures obstruct wind flow. The above elaborations hint the substantial potential of global low-grade wind as well as the strong needs for strategies capable of effectively harvesting low-speed wind energy.

Droplet movement (sliding, bouncing, falling, etc.) actuated by external factors (gravity, drawing, etc.) have been used to harvest energy from raining or mechanical dragging (24–29). A signature of droplet moving is interfacial charge redistribution, which arises because of dynamic deformation and wetting–dewetting compromised by surface tension (30–38). More recently, droplet impacting on superwetting surfaces is adapted to harvest hydraulic power from falling water drops (24). Inspired from these drop-based generators, here, we report a discovery that ionic liquid (IL) droplets sitting on a nanowire array with capillary-stabilized three-phase contact line (TCL) can sensitively turn wind blowing-induced air/liquid interfacial friction into internal rotation, as confirmed by microscope imaging. Our experimental and simulation results reveal that TCL pinning (*SI Appendix*, Fig. S2 and Movie S1), which we create by nanowire array enlarged solid/liquid adhesion hysteresis and advancing contact angle (39–42), geometrically blocks fluid flow at drop/air interfaces. To sustain the cap-shaped drop profile under surface tension and remove excess IL fluid near TCL perimeter, headwind flow arises along the bottom of the drop surrounding the nanowire array. Electrical tests, microscope images, and theoretical calculations together confirm that such IL flow within nanoconfined space spontaneously induces redistribution of positive and negative ions and persistently generates electricity (43), a clear disparate working mechanism from previous studies (44–49). Specifically,

Author contributions: S.Z. designed research; S.P., B.X., Y.W., M.W., X.C., X.J., N.H., H.H., and S.Z. performed research; S.P., B.X., Y.W., M.W., X.C., C.Z., G.L., H.H., and S.Z. contributed new reagents/analytic tools; S.P., B.X., Y.W., M.W., X.C., D.W., R.H., Z.M.W., N.H., H.H., Y.D., and S.Z. analyzed data; and S.P., B.X., M.W., N.H., Y.D., and S.Z. wrote the paper.

The authors declare no competing interest.

This article is a PNAS Direct Submission.



[1]S.P., B.X., and Y.W. contributed equally to this work.

[2]To whom correspondence may be addressed. Email: nanhu026@scut.edu.cn, hyhe@ipe.ac.cn, or zhengshuang@iccas.ac.cn.

This article contains supporting information online at https://www.pnas.org/lookup/suppl/doi:10.1073/pnas.2303466120/-/DCSupplemental.

Published September 11, 2023.

water molecule breaks intimate ion pair and differentiate interactions of cations and anions with chemically modified nanowire walls, which further gives rise to ion redistribution driven by directional flows for power generation (50–53).

## Fundamental Concept and Preliminary Power Output of the Drop Wind Generators (DWGs)

Our DWG comprises a meniscus-shaped fluid droplet consisting of moisture-saturated IL 3-Methyl-1-octylimidazolium chloride (water content $w_{H_2O} \approx 23.3\%$ under relative humidity $\varphi \approx 40\%$) with the contact angle CA = 61 ± 7° (Fig. 1*A*), selected because of the inherent nonvolatility and the sensitivity of ion pairs to air moisture (54). The poly (sodium styrene sulfonate) (PSS) grafted polydimethylsiloxane (PDMS) nanowire arrays have a height $h \approx$ 1.1 μm, diameter $d$ = 91.5 ± 8.7 nm, and center-to-center spacing $P$ = 97.3 ± 13.2 nm (Fig. 1 *B* and *C* and *SI Appendix*, Fig. S3), roughly consistent with the nanoporous anodized aluminum (AAO) mold (*SI Appendix*, Fig. S4). Our strategy for associating IL droplet and wind to produce electricity is on the grounds of the sulfonic acid group to enhance the surface charge (*SI Appendix*, Fig. S5). Compared with bare PDMS, FTIR spectrum of PSS-grafted PDMS presents four additional peaks, of which 1,125 and 1,040 $cm^{-1}$ are assigned to antisymmetric vibration absorption peaks of sulfonate, while the peaks positioned at 1,500 and 1,644 $cm^{-1}$ are ascribed to C-H vibration peaks of the aromatic ring (Fig. 1*D*) (55, 56). These results, together with X-ray photoelectron spectroscopy (XPS) characterization (*SI Appendix*, Fig. S6), strongly indicate successful grafting of PSS brushes onto PDMS nanowires. Subsequently, the wind-induced open-circuit voltage $U_{oc}$ and short-circuit current $I_{sc}$ are independently plotted in Fig. 1*E* as a function of time. Under $\varphi \approx 40\%$ and $V_{wind} \approx 2$ m/s, our device can produce a continuous $U_{oc}$ of ~0.4 V and $I_{sc}$ of ~20 μA, collected with Ag/AgCl electrodes (*SI Appendix*, Figs. S7 and S8). The voltage variations in the cyclic wind-on and wind-off conditions show that $U_{oc}$ repeatedly increases to approximately 0.4 V and decreases to ~0 V, exactly responding to surrounding wind (Fig. 1*F*), indicating that our power generation mechanism is greatly associated with wind flows.

**Wind-Induced Electricity Generation of DWG.** To figure out the working mechanism of DWG, we perform in situ optical microscopic analyses by recording suspended polystyrene (PS) microsphere movements (57) within the IL droplet. Circulating rotation of PS microspheres (Fig. 2 *A* and *B* and Movie S2), under $V_{wind}$ of ~2 m/s, visually demonstrates the generated directional flow against wind from the edge to center surrounding the PDMS substrate, which may give rise to continuous power generation. As shown in Fig. 2*B*, we observe from the left side of the droplet with a focus alignment into its bottom microsphere layer using an optical microscope. The artificial wind blows from the right side with the angle between PDMS substrate and wind flow $\alpha$ = 0°. We find from Fig. 2*A* that the microspheres at the upper layer (fuzzy in i) move following the wind toward left TCL ii).

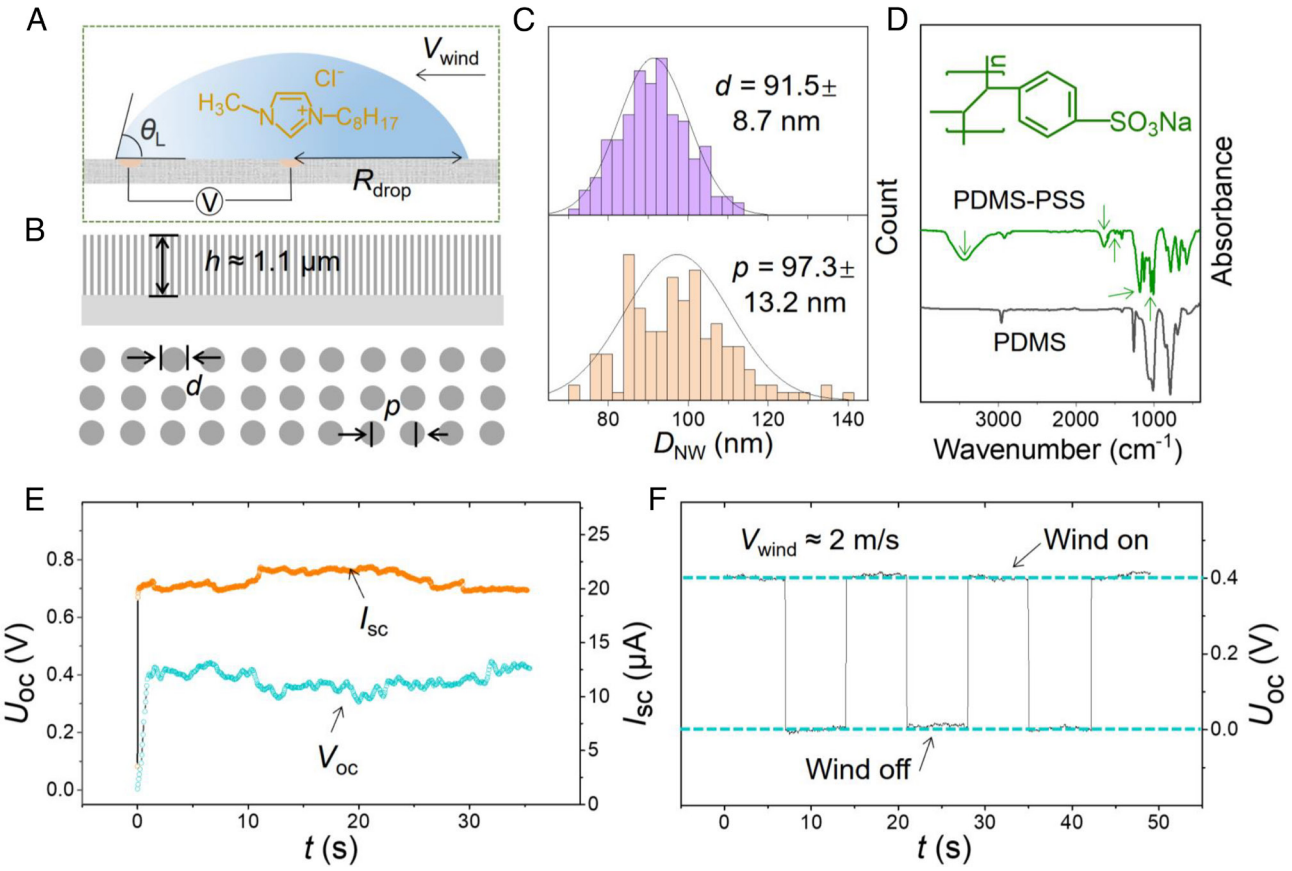


**Fig. 1.** Schematic illustration and power generation capacity of DWG. (*A*) Designing details of the generator, involving the ionic liquid drop seated on modified polydimethylsiloxane (PDMS) nanowire arrays under directional wind. (*B*) Schematic diagram showing the nanowire height ($h$), diameter ($d$), and center-to-center spacing ($p$). (*C*) Distribution statistics of $d$ and $p$ of the modified nanowire array. (*D*) FTIR spectra of PDMS nanowires before and after being grafted with sodium polybenzene sulfonate (PSS) brushes. (*E*) Continuous evolution of open-circuit voltage $U_{oc}$ (green line) and short-circuit current $I_{sc}$ (orange line) output from DWG device when relative humidity $\varphi$ = 40% and wind speed $V_{wind} \approx 2$ m/s. (*F*) Controllable $U_{oc}$ changes with cyclic wind on and wind off operations.

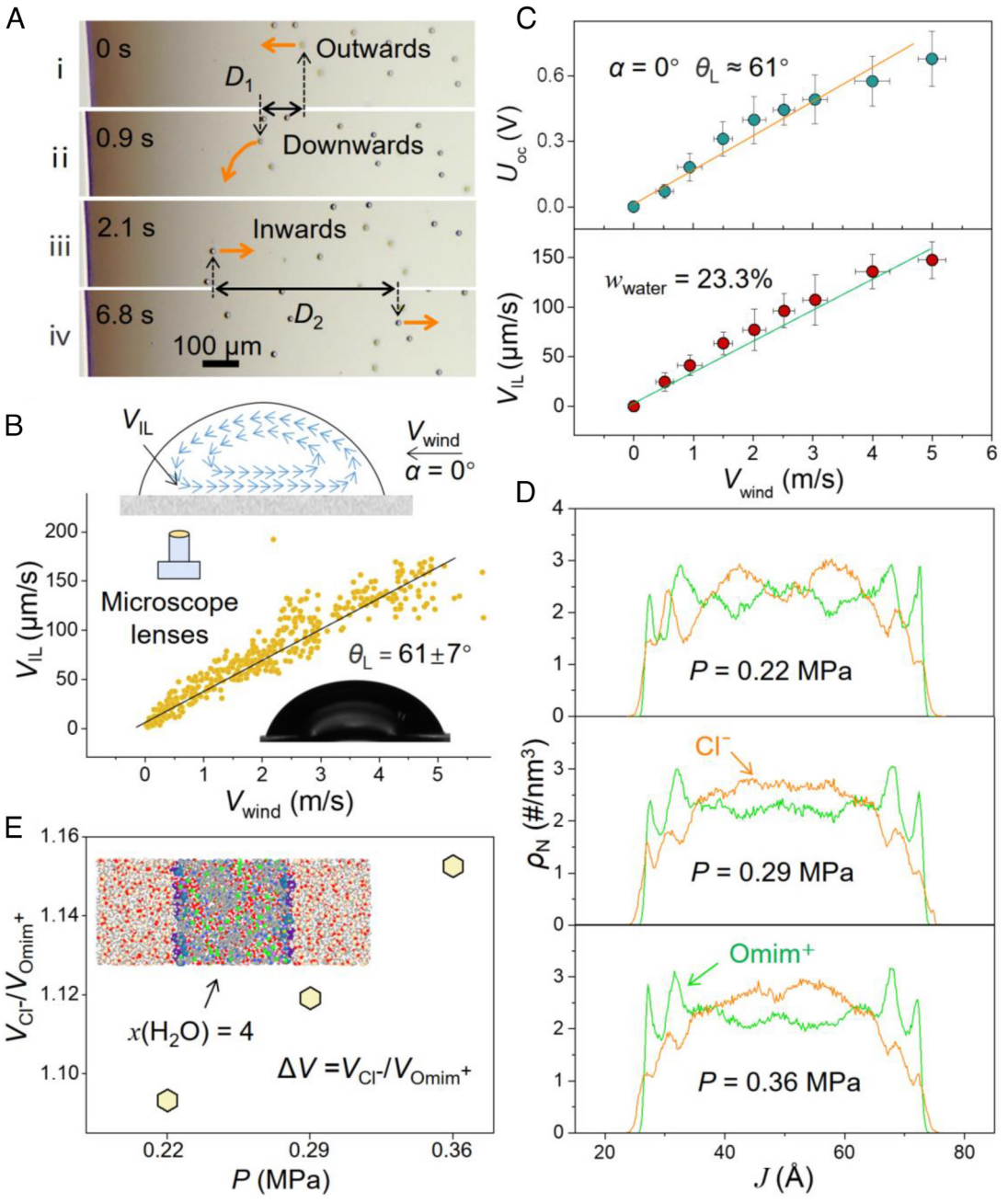


**Fig. 2.** Optical microscope observation and simulations of wind-induced electricity generation from DWG. (*A*) In situ microscope recording of PS microspheres (diameter of ~10 μm) suspended into IL drop ($w_{H_2O} \approx 23.3\%$) under $V_{wind} \approx 2$ m/s to demonstrate the circulating flow. (*B*) Flow velocity $V_{IL}$ ($D_2/t_2$) plotted against wind speed. The *Insets* are CA image of IL placed on PDMS nanowires substrate and the schematic of our device. (*C*) Averaged $U_{oc}$ and $V_{IL}$ versus $V_{wind}$ under $\alpha = 0°$ and CA $\theta_L \approx 61°$. (*D*) The number density $\rho_N$ distribution of $Cl^-$ and $Omim^+$ for confined ILs under pressure of 0.22, 0.29, and 0.36 MPa, respectively. (*E*) The velocity difference between anion and cation for confined ILs as a function of the external pressure. The *Inset* is the simulation model. The color of gray, white, red, bright blue, orange, and green represent the atom of C, H, O, N, Si, and Cl. Meanwhile, the dark purple, olive green, dark blue, and light purple represent the atom of C, S, O, and Na in the sodium benzene sulfonate group.

Then, the microspheres sink down to the bottom near the drop edge and become clear iii). Finally, along the bottom of the droplet, the particles move against the wind direction from the left TCL to the center of the droplet iv). We trace out the complete internal circulation (Fig. 2*B*) by microscope observation at various situations.

To provide deeper insight into how DWG converts wind blowing into electricity, we further quantify $V_{IL}$ and $U_{oc}$ dependence of $V_{wind}$ under $\varphi \approx 40\%$ with the equilibrium $w_{H2O}$ of ~23.3% (Fig. 2*C*). We find that both $U_{oc}$ and flow velocity inside the IL drop $V_{IL}$ exhibit a positive dependence on wind speed. For example, $V_{IL}$ at the wind speed of 5 m/s is ~150 μm/s, almost three orders of magnitude greater than the $V_{IL}$ under $V_{wind} \approx 1$ m/s, with the $U_{oc}$ significantly improved up to ~0.68 V. These results experimentally hint that wind-triggered internal circulating flow may play a critical role in the energy conversion mechanism.

To confirm the above hypothesis, we carry out molecular dynamics (MD) simulations, where the flow speed is equivalent to the applied force in the droplet. Fig. 2*D* shows the density distribution of anions and cations in the 5.34-nm nano space in consistence with our nanowire sizes. Due to differentiated interactions between

[Omim]Cl and nanowire surfaces, the distribution of $Omim^+$ and $Cl^-$ within the nanoconfined space is quite different, which is further enlarged with wind speed increase. In detail, we find that as $V_{wind}$ increases, binding of $Cl^-$ is decreased because $Cl^-$ tends to accumulate in the bulk IL droplet. While on the contrary, $Omim^+$ surrounding nanowire surface increases. To clarify this, we further calculate the speed difference between $Omim^+$ and $Cl^-$ under different pressure. Fig. 2*E* demonstrates that the velocity difference (simulated $\Delta V$) between anions and cations is 1.09, 1.119, and 1.15 for applied pressure within the IL system of 0.22, 0.29, and 0.36 MPa, respectively. These results indicate that increasing the flow velocity will cause enlarged distribution differences of ions and further expand the velocity difference of anions and cations for electricity generation. This enhancement can be attributed to the strong adsorption of water to anion.

**Environmental RH-Mediated Power Generation of DWG.** To further validate the abovementioned working mechanism and gain an insight into the relation between energy conversion performance and ambient environment, our DWG is exposed to air with controlled temperature (25 °C) and RH of ~0, 40, and 60%, respectively, for 2 d to ensure fully adsorption of water (*SI Appendix,* Fig. S9). Thereafter, we measure the equilibrium $w_{H2O}$ (~0, 23.3, and 38.4%) and calculate the corresponding water molar ratio defined as $x(H_2O)$ = mol($H_2O$)/mol(IL) (0, 4, and 8). We find from Fig. 3*A* that DWGs within higher RH behave much better with low-grade wind ranging from 0 to ~5 m/s. For example, when $V_{wind} \approx 5$ m/s, $U_{oc}$ is ~0, 0.68, and 0.84 V as $x(H_2O)$ is, respectively, 0, 4, and 8, suggesting that electricity production is closely associated with the presence of water in the DWG droplet. In our opinion, these results can be ascribed to two main reasons. First, higher RH causes larger water adsorption, resulting in higher water content within IL drop and correspondingly reduce viscosity (58), which finally improves the fluidity and flow velocity inside the IL drop. As illustrated in Fig. 3*B*, when $V_{wind} \approx$ 5 m/s, $V_{IL}$ increases from ~75 to ~163 μm/s as $x(H_2O)$ improves from 0 to 8. Second, water molecules may help to differentiate the interactions between modified PDMS substrates and $Omim^+/Cl^-$ and further enhance the energy conversion performance. To confirm this, we randomly record $U_{oc}$ dependance of $V_{IL}$ as shown in Fig. 3*C*. We find that under the same flow velocity such as ~60 μm/s, $U_{oc}$ fluctuates in the range of 0.13 to 0.31 V when $x(H_2O) \approx 4$, and it is enhanced to 0.23 to 0.41 V when $x(H_2O) \approx 8$.

To validate our hypothesis that water molecules differentiate the interactions between PSS-grafted PDMS and $Omim^+/Cl^-$, we conduct MD simulations with different water contents. Fig. 3*D* shows that the density distribution of anions and cations when the applied force of water molecules contained in the device is 0.29 MPa. When the system is water-free, there is little difference in the distribution of anions and cations because of the strong interactions between $Omim^+$ and $Cl^-$. When the water content of the system increases, the difference in the distribution of anion–cation inside the droplet increases, resulting in the enlarged velocity difference as shown in Fig. 3*E*. That is, when $x$ = 0, 4, and 8, the velocity difference $\Delta V$ of anion-cation is 1, 1.119, and 1.215, which accords well with our experimental results.

**Experimental and Simulation Studies of Wind Directions Mediated Power Generation.** Fig. 4 *A* and *B* plot the variation and mean average of measured voltage in experiments over a span of 100 s, which indicate intensive circulation inside anchored droplets under a given airflow. For the airflow coming from the righthand side ($\alpha$ = 0°) and the lefthand side ($\alpha$ = 180°), a counterclockwise loop and a clockwise loop form, respectively, inside the anchored droplets (*SI Appendix,* Fig. S10 and Movie S3), leading to roughly identical voltage values with an opposite sign (~0.4 V and −0.4 V). Yet, the airflow coming from the top ($\alpha$ = 90°) results in two symmetric loops inside the droplet (*SI Appendix,* Fig. S11 and Movie S4). Therefore, the direction of the airflow plays an important role in the formation of circulating fluid behavior and electricity output.

To reveal the physical principle behind the phenomenon, we conduct numerical simulations through computational fluid dynamics (CFD) modeling using the commercial software Ansys WorkBench R19.0 (*SI Appendix,* Fig. S12). The CFD model provides a numerical approximation to the equations that govern fluid motion, which is an efficient approach to solve differential equations by discretizing the fluid domain. We adopt the volume of fluid (VOF) method to build simplified two-dimensional models for the wind flow around the stationary droplet (see *SI Appendix, Methods* for details). We select Navier–Stokes (NS) equations to describe the dynamic motion of the fluid mixture assumed to be homogeneous and incompressible, consisting of the governing mass and momentum equations as follows:

$$\frac{\partial \rho}{\partial t} + \nabla \cdot (\rho v) = S_m, \quad [2]$$

$$\frac{\partial (\rho v)}{\partial t} + \nabla \cdot (\rho v v) = -\nabla \mathrm{p} + \nabla \cdot \left[\mu \left(\nabla \mathrm{v} + (\nabla \mathrm{v})^{\mathrm{T}}\right)\right] + \rho \mathrm{g} + \mathrm{f}, \quad [3]$$

where $v$ is the velocity vector, $p$ is the pressure, $S_m$ is the mass source item, $f$ is the other volumetric force, $g$ is the acceleration of gravity, $\rho$ is the fluid mixture density, and $\mu$ is the fluid mixture viscosity defined by the VOF model for our multiphase flow problem.

Similar to the experimental results, we observe the exact same rotation directions inside anchored droplets under the airflow with $\alpha$ = 0°, 90°, and 180°, as shown in Fig. 5 *A*–*C*. Our numerical results also provide a map of the velocity field nearby the surface of the droplet, and a slower velocity is identified close to the droplet surface due to interfacial friction. This friction force induces shear stress ($\tau_{IL/air}$) at the air–droplet interface, which drives the inner circulation of the anchored droplets. When $\alpha$ is equal to 0° and 180°, the $\tau_{IL/air}$ value along the circumferential direction increases from the bottom corners and reaches the largest value at the top. The $\tau_{IL/air}$ value on the windward side and corresponding shear stress becomes smaller due to resistance, and the center of the vortex inside the droplet thus moves slightly to the leeward side. When $\alpha$ is equal to 90°, a symmetric airflow passes around the droplet surface, resulting in a symmetric $\tau_{IL/air}$ distribution that leads to two vortex flows inside the droplet.

These findings are derived from the use of a nanowire array, which serves to stabilize the TCL and restrict the movement of fluidic IL within a defined boundary. Previous research has indicated that the coffee ring effect, whereby a droplet's outer edge exhibits a ring-like deposit, occurs due to the geometric constraints imposed by a pinned TCL. This constraint forces the fluid to be pushed outward to compensate for evaporative losses. The pinned TCL prevents the drop's radius from shrinking, necessitating outward liquid flow to prevent drop shrinkage. The pinning of the TCL is facilitated by surface irregularities and is particularly pronounced when solutes are present, as evidenced in previous studies (59, 60). Similarly, in our proposed system, the immobilized TCL assists in restricting the expansion of the droplet when exposed to wind. Consequently, this leads to an accumulation of IL at the downwind position of the droplet. In contrast, an upwind IL flow is established to remove excess fluid and maintain the cap-shaped droplet, with the process being regulated by surface tension. In Fig. 5*D*, we also conduct a parametric study

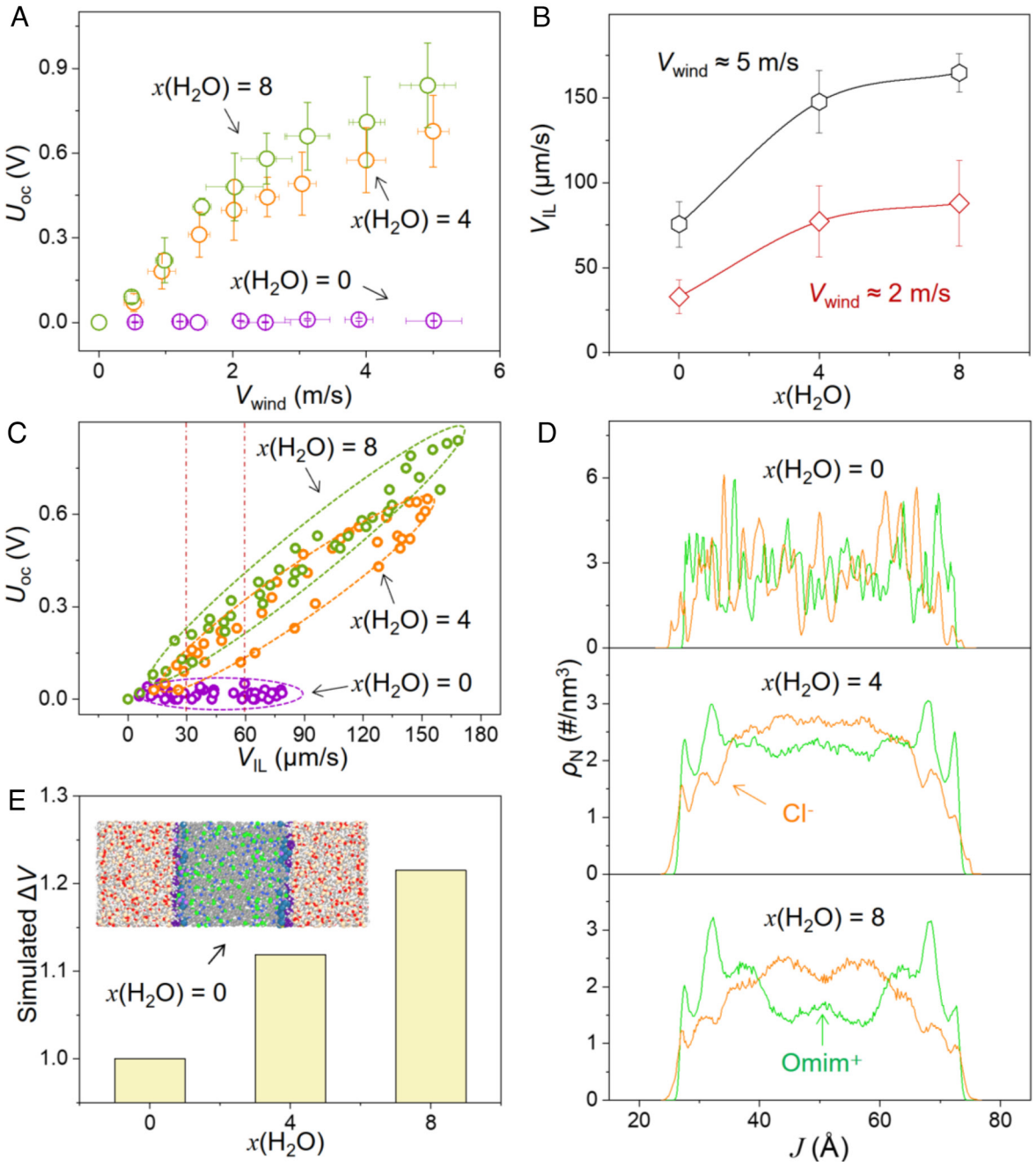


**Fig. 3.** RH regulated power generation of DWG. (*A*) $U_{oc}$ variation of DWG with incremental wind speed when $x(H_2O)$ is 0, 4, and 8, respectively. (*B*) $V_{IL}$ variation versus $x(H_2O)$ under $V_{wind}$ of 2 and 5 m/s, respectively. (*C*) $U_{oc}$ versus $V_{IL}$ under $x(H_2O)$ of 0, 4, and 8, respectively. (*D*) The number density distribution of $Cl^-$ and $Omim^+$ for confined ILs with $x(H_2O)$ of 0, 4, and 8, respectively. (*E*) The velocity difference between anion and cation for confined ILs as a function of $x(H_2O)$.

to identify the effect of the airflow speed on the average velocity ($V_{IL}$) along the bottom surface inside the droplet which is associated with the velocity of the vortex. The CFD model estimates a linear increase of the velocity as the airflow intensity becomes larger. Guided by our simulation, we conduct a testing series and normalize the absolute values for comparison. We find that the normalized $V_{IL}$ values (Fig. 5*E*) and $U_{oc}$ (Fig. 2*C*) in experiments show a similar trend as simulation results.

Having validated of our CFD model and understood the mechanics behind the circulation inside the anchored droplet, we further evaluate the effect of droplet profiles on the resulting behavior of the droplet. *SI Appendix,* Fig. S14*A*, presents five anchored droplets in an experimental series with various contact angles $\theta_L$. We gradually reduce the apparent CA by removing IL from the drop, and five angles are approximately tested ranging from 11° to 51°. The measured relationship between their drop heights and $\theta_L$ is plotted in *SI Appendix,* Fig. S14*B*, showing a linear increase through a procedure of geometries generation (see SI Appendix, *Methods* for details). We take advantage of our CFD model and compare the distribution of shear stress $\tau_{IL/air}$ on the air–droplet interface under the same airflow with $\alpha$ = 0°. Numerical results shown in *SI Appendix,* Fig. S14*C*, indicate that as the $\theta_L$ decreases, the shear stress distributions become smaller. A smaller shear stress distribution would lead to a lower circulation velocity inside the droplet which is associated with reduced energy conversions (*SI Appendix,* Fig. S15). This trend was also observed in the experiment as indicated in *SI Appendix,* Fig. S14*D*, where the normalized velocities in the simulation and experiment agree very well. Nevertheless, energy conversion is still

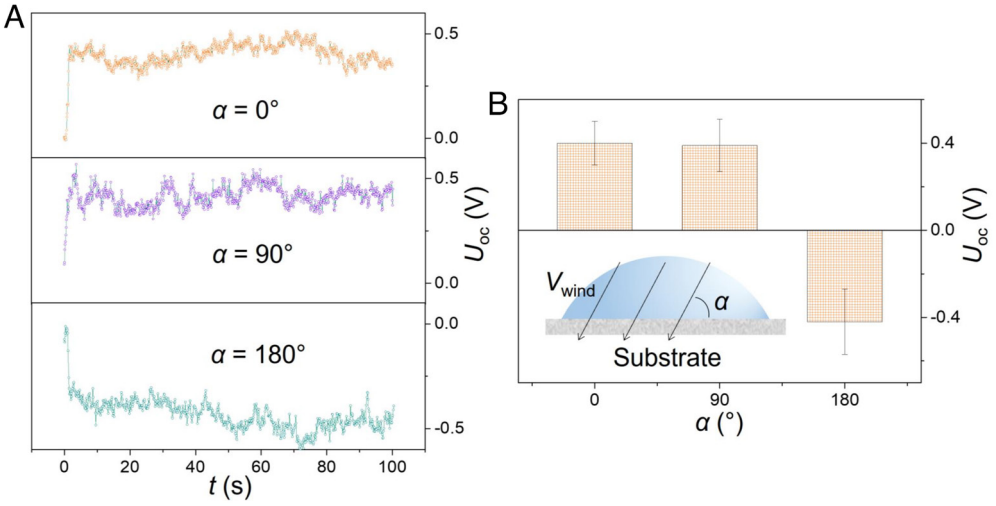


**Fig. 4.** Wind directions mediated energy conversion. (*A*) $U_{oc}$ recording of DWG with $\alpha$ = 0°, 90°, and 180°, respectively. (*B*) Averaged $U_{oc}$ versus wind directions $\alpha$. The *Inset* is a schematic illustration of $\alpha$, the angle between PDMS substrate and wind flow.

possible for anchored droplets with different geometries, although their capacity might be changed.

Finally, we illustrate utility of low-grade wind as a promising energy resource through drop wind farms for powering electronics, such as liquid crystal display (LCD) screens. First, we show scalability of DWG by connecting IL drop in series. Wind farms comprising 81 drops can supply an open-circuit voltage approaching ~60 V under the RH $\varphi \approx 65\%$ (*SI Appendix,* Fig. S14*E*). In addition, we use three drops to light up LCD screens for digital computation (*SI Appendix,* Fig. S14*F* and Movie S5). All these results confirm that our energy conversion strategy works still well for practical applications.

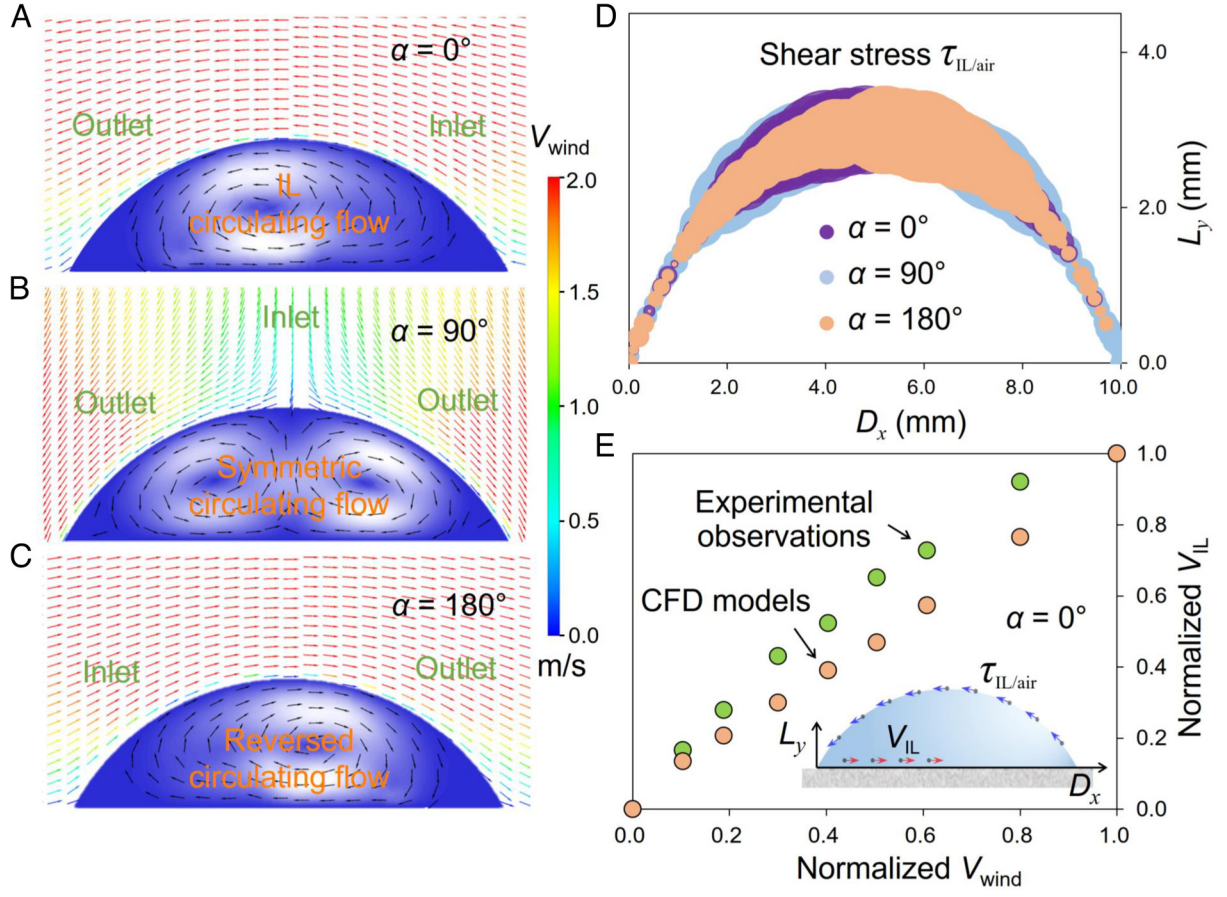


**Fig. 5.** Internal circulation and shear stress distribution of the anchored droplet. (*A*–*C*) The simulated single and double circulation inside the anchored droplets driven by the external airflow with an angle of $\alpha$ = 0°, 90°, and 180°, respectively (*SI Appendix,* Fig. S13). (*D*) Simulated shear stress ($\tau_{IL/air}$) distribution on the droplet surface that demonstrates the drive of internal flow fields inside the droplet. (*E*) Comparison of normalized average velocity in experiments and simulation at the bottom edge of the anchored droplet when $\alpha$ = 0°.

## Conclusions

Overall, our experimental and theoretical results shown above support our hypothesis that directional circulating flow within the anchored IL droplet created by external airflow in any directions can be adapted to trigger cooperative process involving surface charge redistribution and continuous low-speed wind energy conversion, as we have shown in Figs. 2 and 3. We have also designed the modified nanowire array to proactively provide confined space for regulating ion transport and droplet anchoring under wind blowing. Given the widespread distribution and easy accessibility of low-grade wind, these findings expand the great potential of currently untapped low-speed wind as an attractive energy resource for powering electronics, such as LCD screen. Future efforts will be focused on material upgrade to provide well-tuned intermolecular interactions between IL and the solid base supporting the droplet and to enhance flow-directed redistribution of cations and anions for power generation.

## Methods

**Fabrication Method of the PDMS Nanowire Arrays.** PDMS prepolymer hybrid (Dow Corning, Sylgard 184) was fabricated by blending prepolymer and its hardener in a mass ratio of 10:1 and then manually agitating for 10 min and continuously outgassing in vacuum for 30 min. More detailed information about the materials and methods is available in *SI Appendix*.

**Data, Materials, and Software Availability.** All study data are included in the article and/or supporting information.

**ACKNOWLEDGMENTS.** S.Z. acknowledges financial support from the University of Hong Kong (2201100473). S.P. thanks the financial support by the Natural Science Foundation of Hebei Province (E2020201035). N.H. appreciates the financial support from the Guangdong Provincial Key Laboratory of Modern Civil Engineering Technology (2021B1212040003). Y.W. and H.H. thank the funding from the National Natural Science Foundation of China (22278401 and 21890762) and the Youth Innovation Promotion Association of CAS (2021046 and Y2021022). S.P. thanks Professor Hongzan Song and Professor Fengchao Li of Hebei University for the kind help within microscope imaging.

Author affiliations: [a]Department of Inorganic Chemistry, College of Chemistry and Materials Science, Key Laboratory of Medicinal Chemistry and Molecular Diagnosis of Ministry of Education, Key Laboratory of Analytical Science and Technology of Hebei Province, Hebei University, Baoding, Hebei 071002, China; [b]School of Civil Engineering and Transportation, South China University of Technology, Guangzhou 510641, China; [c]Beijing Key Laboratory of Ionic Liquids Clean Process, Institute of Process Engineering, Chinese Academy of Sciences, Beijing 100190, China; [d]Department of Biomedical Sciences, City University of Hong Kong, Hong Kong, China; [e]School of Chemical Engineering, Zhengzhou University, Zhengzhou 450001, China; [f]School of Environmental Engineering, Yellow River Conservancy Technical Institute, Kaifeng 475004, China; [g]Pritzker School of Molecular Engineering, University of Chicago, Chicago IL 60637; [h]Pazhou Lab., Guangzhou 510005, China; [i]Longzihu New Energy Laboratory, Zhengzhou Institute of Emerging Industrial Technology, Zhengzhou 451150, China; [j]School of Chemical Engineering, University of Birmingham, Birmingham B15 2TT, United Kingdom; and [k]Department of Civil Engineering, The University of Hong Kong, Hong Kong, China

1. Statistical Review of World, Statistical review of world energy, 70th edition (2021). http://www.bp.com/en/global/corporrate/energy-economica/statistical-review-of-world-energy.html#tab_sr-2021. Accessed 6 September 2022.
2. M. Arshad, B. O'Kelly, Global status of wind power generation: Theory, practice, and challenges. *Int. J. Green Energy* **16**, 1073–1090 (2019).
3. S. A. Vargas *et al.*, Wind power generation: A review and a research agenda. *J. Clean Prod.* **218**, 850–870 (2019).
4. M. R. Patel, O. Beik, *Wind and Solar Power Systems: Design, Analysis, and Operation* (CRC Press, 2021).
5. V. L. Hartwick, O. B. Toon, J. K. Lundquist, O. A. Pierpaoli, M. A. Kahre, Assessment of wind energy resource potential for future human missions to Mars. *Nat. Astron.* **7**, 298–308 (2022).
6. C. Jung, D. Schindler, Development of onshore wind turbine fleet counteracts climate change-induced reduction in global capacity factor. *Nat. Energy* **7**, 608–619 (2022).
7. L. Kitzing, M. K. Jensen, T. Telsnig, E. Lantz, Multifaceted drivers for onshore wind energy repowering and their implications for energy transition. *Nat. Energy* **5**, 1012–1021 (2020).
8. K. B. Karnauskas, J. K. Lundquist, L. Zhang, Southward shift of the global wind energy resource under high carbon dioxide emissions. *Nat. Geosci.* **11**, 38–43 (2018).
9. G. Russo, Renewable energy: Wind power tests the waters. *Nature* **513**, 478–480 (2014).
10. P. Veers *et al.*, Grand challenges in the science of wind energy. *Science* **366**, eaau2027 (2019).
11. M. Qiu, C. M. Zigler, N. E. Selin, Impacts of wind power on air quality, premature mortality, and exposure disparities in the United States. *Sci. Adv.* **8**, eabn8762 (2022).
12. L. Duan, R. Petroski, L. Wood, K. Caldeira, Stylized least-cost analysis of flexible nuclear power in deeply decarbonized electricity systems considering wind and solar resources worldwide. *Nat. Energy* **7**, 260–269 (2022).
13. E. Rinne, H. Holttinen, J. Kiviluoma, S. Rissanen, Effects of turbine technology and land use on wind power resource potential. *Nat. Energy* **3**, 494–500 (2018).
14. R. Hara, "Prediction of wind power generation output and network operation" in *Integration of Distributed Energy Resources in Power System*, T. Funabashi, Ed. (Academic Press, 2016), chap. 5.
15. V. Patel, D. Guha, S. Purwar, Disturbance Observer-Aided Adaptive Sliding Mode Controller for Frequency Regulation in Hybrid Power System (Academic Press, 2022), chap. 2.
16. L. M. Miller, A. Kleidon, Wind speed reductions by large-scale wind turbine deployments lower turbine efficiencies and set low generation limits. *Proc. Natl. Acad. Sci. U.S.A.* **113**, 13570–13575 (2016).
17. S. R. Venkatramakrishnan, J. Pandey, A. K. Mondal, A. Karn, Low speed wind turbines for power generation: A review. *J. Adv. Res. Fluid. Therm. Sci.* **67**, 146–169 (2020).
18. Y. Zhang *et al.*, An ultra-durable windmill-like hybrid nanogenerator for steady and efficient harvesting of low-speed wind energy. *Nanomicro Lett.* **12**, 175 (2020).
19. S. C. Pryor, R. J. Barthelmie, A global assessment of extreme wind speeds for wind energy applications. *Nat. Energy* **6**, 268–276 (2021).
20. P. Sherman, X. Chen, M. McElroy, Offshore wind: An opportunity for cost-competitive decarbonization of China's energy economy. *Sci. Adv.* **6**, eaax9571 (2020).
21. C. Jung, D. Schindler, Changing wind speed distributions under future global climate. *Energy Convers. Manage.* **198**, 111841 (2019).
22. W. Han, P. Yan, W. Han, Y. He, Design of wind turbines with shroud and lobed ejectors for efficient utilization of low-grade wind energy. *Energy* **89**, 687–701 (2015).
23. W. T. Chong *et al.*, Early development of an innovative building integrated wind, solar and rain water harvester for urban high rise application. *Energy Build.* **47**, 201–207 (2012).
24. W. Xu *et al.*, A droplet-based electricity generator with high instantaneous power density. *Nature* **578**, 392–396 (2020).
25. N. Zhang *et al.*, A universal single electrode droplet-based electricity generator (SE-DEG) for water kinetic energy harvesting. *Nano Energy* **82**, 105735 (2021).
26. Q. Zhang *et al.*, A single-droplet electricity generator achieves an ultrahigh output over 100 V without pre-charging. *Adv. Mater.* **33**, 2105761 (2021).
27. J. Nie *et al.*, Power generation from the interaction of a liquid droplet and a liquid membrane. *Nat. Commun.* **10**, 2264 (2019).
28. D. Yoo *et al.*, Lotus leaf-inspired droplet-based electricity generator with low-adhesive superhydrophobicity for a wide operational droplet volume range and boosted electricity output. *Nano Energy* **99**, 107361 (2022).
29. Z. Ma, J. Ai, Y. Shi, K. Wang, B. Su, A superhydrophobic droplet-based magnetoelectric hybrid system to generate electricity and collect water simultaneously. *Adv. Mater.* **32**, 2006839 (2020).
30. Q. Sun *et al.*, Surface charge printing for programmed droplet transport. *Nat. Mater.* **18**, 936–941 (2019).
31. X. Li *et al.*, Spontaneous charging affects the motion of sliding drops. *Nat. Phys.* **18**, 713–719 (2022).
32. W. Tang, B. D. Chen, Z. L. Wang, Recent progress in power generation from water/liquid droplet interaction with solid surfaces. *Adv. Funct. Mater.* **29**, 1901069 (2019).
33. H. Wu, N. Mendel, D. Van den Ende, G. Zhou, F. Mugele, Energy harvesting from drops impacting onto charged surfaces. *Phys. Rev. Lett.* **125**, 078301 (2020).
34. J. Ju *et al.*, A multi-structural and multi-functional integrated fog collection system in cactus. *Nat. Commun.* **3**, 1247 (2012).
35. A. R. Parker, C. R. Lawrence, Water capture by a desert beetle. *Nature* **414**, 33–34 (2001).
36. W. Xu *et al.*, Triboelectric wetting for continuous droplet transport. *Sci. Adv.* **8**, eade2085 (2022).
37. C. Ye *et al.*, An integrated solar panel with a triboelectric nanogenerator array for synergistic harvesting of raindrop and solar energy. *Adv. Mater.* **35**, 2209713 (2023).
38. A. Stetten, D. Golovko, S. Weber, H. Butt, Slide electrification: Charging of surfaces by moving water drops. *Soft Matter* **15**, 8667–8679 (2019).
39. L. Wen, Y. Tian, L. Jiang, Bioinspired super-wettability from fundamental research to practical applications. *Angew. Chem. Int. Ed.* **54**, 3387–3399 (2015).
40. B. Bhushan, Biomimetics: Lessons from nature-an overview. *Philos. Trans. R. Soc. A* **367**, 1445–1486 (2009).
41. B. Bhushan, Y. C. Jung, K. Koch, Micro-, nano- and hierarchical structures for superhydrophobicity, self-cleaning and low adhesion. *Philos. Trans. R. Soc. A* **367**, 1631–1672 (2009).
42. M. Liu, S. Wang, L. Jiang, Nature-inspired superwettability systems. *Nat. Rev. Mater.* **2**, 17036 (2017).
43. H. Zhu, F. Xia, Catalysis controlled by electro-responsive wetting. *Matter* **5**, 785–787 (2022).
44. X. Liu *et al.*, Power generation from ambient humidity using protein nanowires. *Nature* **578**, 550–554 (2020).
45. J. Tan *et al.*, Self-sustained electricity generator driven by the compatible integration of ambient moisture adsorption and evaporation. *Nat. Commun.* **13**, 3643 (2022).
46. H. Wang *et al.*, Moisture adsorption-desorption full cycle power generation. *Nat. Commun.* **13**, 2524 (2022).
47. Q. Hu, Y. Ma, G. Ren, B. Zhang, S. Zhou, Water evaporation-induced electricity with geobacter sulfurreducens biofilms. *Sci. Adv.* **8**, eabm8047 (2022).
48. H. Wang *et al.*, Bilayer of polyelectrolyte films for spontaneous power generation in air up to an integrated 1000 V output. *Nat. Nanotechnol.* **16**, 811–819 (2021).
49. Y. Lu *et al.*, Liquid-liquid triboelectric nanogenerator based on the immiscible interface of an aqueous two-phase system. *Nat. Commun.* **13**, 5316 (2022).
50. H. Zhu *et al.*, Recent advances in photocatalysis based on bioinspired superwettabilities. *ACS Catal.* **11**, 4751–14771 (2021).

51. Y. Zhao *et al.*, Robust sulfonated poly (ether ether ketone) nanochannels for high-performance osmotic energy conversion. *Natl. Sci. Rev.* **7**, 1349–1359 (2020).
52. Y. He, M. Tsutsui, Y. Zhou, X. S. Miao, Solid-state nanopore systems: From materials to applications. *NPG Asia Mater.* **13**, 48 (2021).
53. A. Serva *et al.*, Structural and dynamic properties of soda–lime–silica in the liquid phase. *J. Chem. Phys.* **153**, 214505 (2020).
54. J. Kong, H. He, Challenge and opportunity of ionic liquids-an interview with prof. Douglas R. Macfarlane. *Green Energy Environ.* **5**, 243–245 (2020).
55. G. Zundel, Hydration structure and intermolecular interaction in polyelectrolytes. *Angew. Chem. Int. Ed.* **8**, 499–509 (1969).
56. J. C. Yang, M. J. Jablonsky, J. W. Mays, NMR and FT-IR studies of sulfonated styrene-based homopolymers and copolymers. *Polymer* **43**, 5125–5132 (2002).
57. S. Scharnowski, C. J. Kähler, Particle image velocimetry-classical operating rules from today's perspective. *Opt. Laser. Eng.* **135**, 106185 (2020).
58. J. P. Hallett, T. Welton, Room-temperature ionic liquids: Solvents for synthesis and catalysis. 2. *Chem. Rev.* **111**, 3508–3576 (2011).
59. R. Deegan *et al.*, Capillary flow as the cause of ring stains from dried liquid drops. *Nature* **389**, 827–829 (1997).
60. P. Yunker, T. Still, M. Lohr, A. Yodh, Suppression of the coffee-ring effect by shape-dependent capillary interactions. *Nature* **476**, 308–311 (2011).